Heavy-ion optical potentials from few-nucleon transfer reactions*

A. J. Baltz, P. D. Bond, J. D. Garrett, and S. Kahana
Brookhaven National Laboratory, Upton, New York 11973
(Received 10 February 1975)

The sensitivity of forward angle heavy-ion transfer calculations to the details of the imaginary optical potential in the region of the nuclear surface is demonstrated. A phenomenological imaginary potential, consisting of a deep volume term of sharp diffusivity and a shallow surface term of standard diffusivity, is proposed and used in distorted-wave Born-approximation calculations to reproduce a variety of angular distribution shapes. The proposed parametrization of the imaginary potential allows the region of the nuclear surface to be transparent enough to produce large forward angle cross sections, seen experimentally, and yet remain strongly enough absorbing in the nuclear interior to suppress unphysical contributions from this region. Bound state configuration dependence of angular shapes, produced in two-particle transfer calculations with weakly absorbing volume potentials, is shown to be removed by the use of the proposed surface transparent potentials.

[NUCLEAR REACTIONS DWBA analysis of $\sigma(\theta)$ for ^{40}Ca(^{13}C, ^{14}N), $E=40$ MeV; ^{40}Ca(^{13}C, ^{12}C), $E=40$, 60, and 68 MeV; ^{48}Ca(^{14}N, ^{13}C), $E=50$ MeV; ^{60}Ni(^{18}O, ^{16}O), $E=65$ MeV; ^{60}Ni(^{18}O, ^{19}F), $E=65$ MeV. Discussion of optical-model parameters for such reactions.]

I. INTRODUCTION

Forward angle cross sections of heavy-ion induced transfer reactions are the subject of numerous recent studies (c.f. Refs. 1–10). At incident energies sufficiently above the Coulomb barrier these forward angle cross sections can be large, and the angular position of the most forward peak is dependent upon the transferred angular momentum.[2,6,8] It has been demonstrated (see e.g., Refs. 1–4, 7) that the magnitude of these forward cross sections is particularly sensitive to the absorptive potential at the nuclear surface. In many cases it is possible to reproduce such forward angle cross sections with DWBA calculations using weakly absorbing optical-model potentials with the same Woods-Saxon geometry in the real and imaginary wells. These potentials also reproduce the elastic scattering cross sections and the magnitude and energy dependence (for a limited range of incident energies) of single-nucleon transfer cross sections.[2,3]

However, angular distributions for reactions at reasonably low energies (~1.5 times the barrier), which have a well formed "bell-shaped" peak at the grazing angle and large forward angle peaks, are often difficult to reproduce using Woods-Saxon wells of the same geometry. The use of different geometries for the real and imaginary potentials to fit data[1,6,10,11] is not new, but little justification or discussion of the effects of such potentials has been given. The present paper discusses the importance of heavy-ion transfer angular distributions in limiting the allowed shape of the imaginary potential. The proposed potentials,[12] which are not unique, but whose general features are required by the data, consist of a strongly absorbing volume part with a small diffusivity and a surface absorptive potential with a more standard diffusivity. The volume potential must be deep enough to effectively exclude flux from the interior and yet reduced in radius and sharp enough to allow surface processes. The inclusion of the surface potential is based on physical arguments and accounts for loss of flux to quasielastic processes, which can account for a significant fraction of the total reaction cross section.[13,14] Calculations using such potentials reproduce the shape and magnitude of selected one- and two-nucleon transfer angular distributions as well as elastic scattering.

II. ANALYSIS

The distorted-wave Born-approximation (DWBA) single-nucleon transfer cross section, $\sigma_{\mathrm{DWBA}}(\theta)$, calculated for the reaction $A(a,b)B$ is related to the experimental stripping cross section $\sigma_{\mathrm{exp}}(\theta)$ through spectroscopic factors

$$\sigma_{\mathrm{exp}}(\theta) = NC^2S_{ab}C^2S_{AB}\sigma_{\mathrm{DWBA}}(\theta)\,. \tag{1}$$

Differential cross sections for the single-nucleon transfer studies discussed below were calculated using the finite range DWBA code SRC.[15] This code includes the effects of recoil in a proper Taylor series expansion[16] keeping terms to the second order. Values assumed for the spectroscopic factors, taken from light-ion experimental measurements[17–21] or from theoretical calculation,[22] are

TABLE I. Values of the spectroscopic factors assumed in the analysis.

Case	C^2S	Source	Ref.
$^{13}C_{g.s.} \rightarrow {}^{12}C_{g.s.} + n$	0.77	ave. of $^{12}C(d,p)$	17
$^{13}C_{g.s.} + p \rightarrow {}^{14}N_{g.s.}$	0.69	theory	22
$^{14}N_{g.s.} \rightarrow {}^{13}C_{g.s.} + p$	0.69	theory	22
$^{18}O_{g.s.} + p \rightarrow {}^{19}F_{g.s.}$	0.30	$^{18}O(^3He, d)$	18
$^{18}O_{g.s.} + p \rightarrow {}^{19}F_{0.11}$	0.12	$^{18}O(^3He, d)$	18
$^{18}O_{g.s.} + p \rightarrow {}^{19}F_{0.20}$	0.42	$^{18}O(^3He, d)$	18
$^{40}Ca_{g.s.} \rightarrow {}^{39}K_{g.s.} + p$	4.0	sum rule	...
$^{40}Ca_{g.s.} + n \rightarrow {}^{41}Ca_{g.s.}$	0.80	$^{40}Ca(d,p)$	19
$^{48}Ca_{g.s.} + p \rightarrow {}^{49}Sc_{g.s.}$	1.0	$^{48}Ca(^3He, d)$ and (d,n)	20
$^{48}Ca_{g.s.} + p \rightarrow {}^{49}Sc_{3.08}$	0.60	$^{48}Ca(^3He, d)$ and (d,n)	20
$^{60}Ni_{g.s.} \rightarrow {}^{59}Co_{g.s.} + p$	6.0	ave. of $^{60}Ni(t, \alpha)$ and $(d, {}^3He)$	21

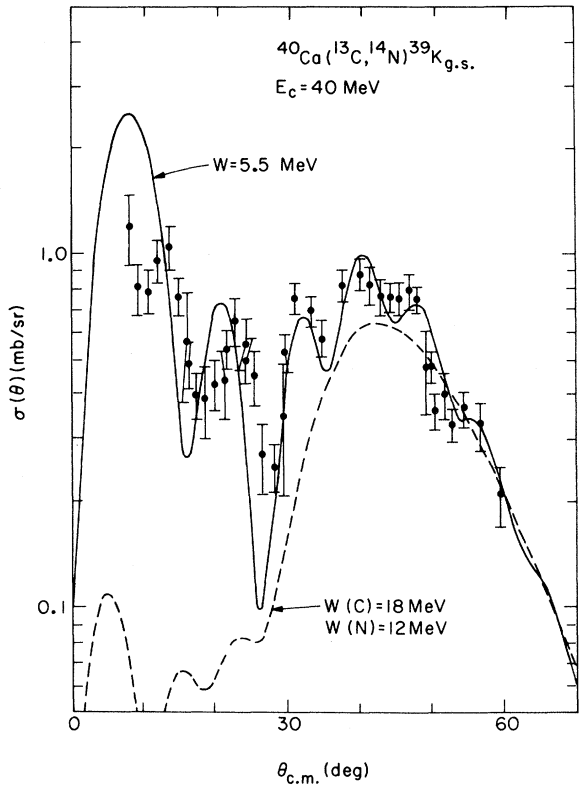

FIG. 1. Angular distribution of the $^{40}Ca(^{13}C, {}^{14}N)$ transition to the ground state of ^{39}K measured at an incident energy of 40 MeV (from Refs. 25 and 26). The dashed curve, calculated using optical-model parameters (Set 2, Table II) derived from a fit to 40 MeV elastic scattering of both ^{13}C and ^{14}N on ^{40}Ca, fails to reproduce the large, rapidly varying experimental angular shape at forward angles. With the absorption reduced to $W = 5.5$ MeV in both entrance and exit channels, large cross sections are predicted (solid curve) at forward angles; however, the details of the oscillating yield still are not reproduced.

given in Table I. A value of the normalization constant N near one then indicates agreement between the predicted and measured cross sections.

The $^{60}Ni(^{18}O, {}^{16}O)^{62}Ni$ cross sections were calculated using the two-nucleon transfer version[23] of the finite range DWBA code RDRC.[24] This code calculates the two-nucleon transfer form factor microscopically, but the effects of recoil are not included.

III. DISCUSSION

A. 40 MeV $^{40}Ca(^{13}C, {}^{14}N)^{39}K$(g.s.) angular distribution

An angular distribution shape typical of those difficult to reproduce by DWBA calculations using conventional heavy-ion optical potentials is shown in Fig. 1. It corresponds to the $^{40}Ca(^{13}C, {}^{14}N)$ transition to the ^{39}K ground state, $J^\pi = \frac{3}{2}^+$, measured[25,26] at an incident energy of 40 MeV. A large rapidly varying differential cross section is observed at the most forward angles while smaller amplitude oscillations, superimposed on a broad peak, are observed near angles corresponding to the classical grazing trajectory. Shown with the data are DWBA calculations based on optical-model parameters having identical geometry for both the real and imaginary potential wells. The dashed curve represents calculations based on parameters (Set 2 of Table II) which reproduce ^{13}C and ^{14}N elastic scattering on ^{40}Ca over a range of incident energies.[3,26] This calculation reproduces neither the large forward angle cross section nor the variation of the cross section as a function of angle. If the imaginary potentials in both the entrance and exit channels are reduced to $W = 5.5$ MeV, with the other parameters unchanged, the forward angle cross sections are strongly enhanced and strong oscillations are predicted (solid curve in Fig. 1). However, the oscillations of the curves based on these weakly absorbing potentials are out of phase with the data forward of 30°. The positions of these peaks in the data agree much better with the maxima calculated using the more strongly absorbing potentials.

The change in the angular positions of the forward angle maxima is the result of contributions from amplitudes corresponding to large nuclear overlaps. Calculated angular distributions for the $^{40}Ca(^{13}C, {}^{14}N)^{39}K$(g.s.) reaction (for $W = 5.5$) as a function of the lower radial cutoff radius, R_{co}, are shown in Fig. 2, clearly indicating that contributions from the nuclear interior are present. In fact, large contributions to the calculated forward angle cross section come from separations of the nuclear centers of less than 5 fm, causing the po-

TABLE II. Optical-model parameters used in calculations:

$$U(r) = V_c - V\frac{1}{1+e^{x}} - iW_{WS}\frac{1}{1+e^{x'}} + iW_{SD}4a'_{SD}\frac{d}{dr}\left(\frac{1}{1+e^{x''}}\right)$$

where

$$x = \frac{r-R}{a}, \quad x' = \frac{r-R'_{WS}}{a'_{WS}}, \quad x'' = \frac{r-R'_{SD}}{a'_{SD}}.$$

Channel		V (MeV)	R (fm)	$a=a'_{SD}$ (fm)	W_{WS} (MeV)	W_{SD} (MeV)	R'_{WS} (fm)	R'_{SD} (fm)	a'_{WS} (fm)
			^{40}Ca(^{13}C, ^{14}N)^{39}K Reaction						
^{13}C+^{40}Ca	Set 1	33.4	7.33	0.55	18	4.5	6.75	6.75	0.05
	Set 2	33.4	7.33	0.55	18	···	7.33	···	0.55
	Set 3	33.4	7.33	0.55	10	···	7.33	···	0.20
^{14}N+^{39}K	Set 1	34.2	7.37	0.55	18	0.3	7.10	7.10	0.05
	Set 2	34.2	7.37	0.55	12	···	7.37	···	0.55
	Set 3	34.2	7.37	0.55	12	···	6.70	···	0.20
			^{40}Ca(^{13}C, ^{12}C)^{41}Ca Reaction						
^{13}C+^{40}Ca	40 MeV	33.4	7.33	0.55	18	4.5	6.75	6.75	0.05
	60 MeV	33.4	7.33	0.55	18	9.0	6.90	6.90	0.05
	68 MeV	33.4	7.33	0.55	18	9.0	7.00	7.00	0.05
^{12}C+^{41}Ca	40 MeV	33.4	7.29	0.55	18	4.5	6.75	6.75	0.05
	60 MeV	33.4	7.29	0.55	18	9.0	6.90	6.90	0.05
	68 MeV	33.4	7.29	0.55	18	9.0	7.00	7.00	0.05
			^{48}Ca(^{14}N, ^{13}C)^{49}Sc Reaction						
^{14}N+^{48}Ca		70.0	7.47	0.50	18	8.0	7.00	7.00	0.05
^{13}C+^{49}Sc		70.0	7.33	0.50	18	8.0	7.00	7.00	0.05
			^{60}Ni(^{18}O, ^{16}O)^{62}Ni Reaction						
^{18}O+^{60}Ni	Set 1	70	8.68	0.40	18	1	8.38	8.68	0.05
	Set 2	70	8.68	0.40	8	···	8.20	···	0.50
^{16}O+^{62}Ni	Set 1	70	8.31	0.40	18	1	8.01	8.31	0.05
	Set 2	70	8.31	0.40	8	···	8.20	···	0.50
			^{60}Ni(^{18}O, ^{19}F)^{59}Co Reaction						
^{18}O+^{60}Ni		70	8.68	0.40	18	1	8.38	8.68	0.05
^{19}F+^{59}Co		70	8.71	0.40	18	1	8.40	8.71	0.05
			Bound state						
^{40}Ca(^{13}C, ^{14}N)^{39}K [a]			$1.2A^{1/3}$	0.65	···	···	···	···	···
^{40}Ca(^{13}C, ^{12}C)^{41}Ca [a]			$1.2A^{1/3}$	0.65	···	···	···	···	···
Other reactions [a]			$1.25A^{1/3}$	0.65	···	···	···	···	···

[a] The bound state well depths were adjusted to give the transferred nucleon the proper binding energy.

sitions of the forward maxima to shift as the nuclear interior is included.

With the absorptive potential weak throughout the nuclear volume, the lower partial waves have a significant effect upon the cross section. In Fig. 3 the transition amplitudes,[27] β_l^{LM}, as a function of the outgoing partial wave l are shown for the $M=1$ normal and $M=2$ non-normal substates. The diffraction pattern of the solid curve in Fig. 1 arises from a beating of the contributions corresponding to the two peaks in β_l^{LM} shown in Fig. 3. When the first 15 partial waves are removed, the angular positions of the maxima return to those calculated using the strongly absorptive potential (see Fig. 4).

In addition to the desire to reproduce the phase of the data, there is a strong theoretical prejudice against allowing interior contributions to a one step direct heavy-ion process. Large overlap of the two ion densities surely implies that more complex processes are dominant, and indeed the optical model itself is no longer relevant. The absorption in the

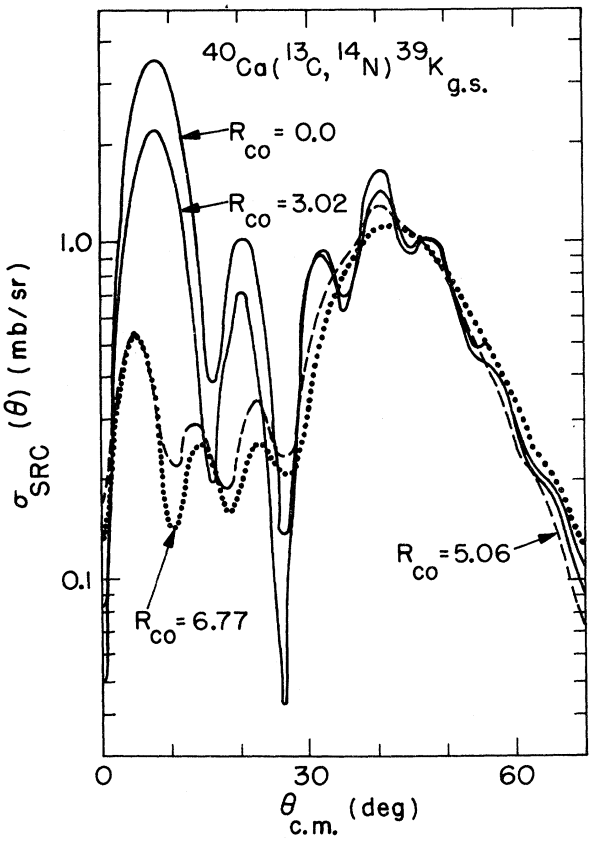

FIG. 2. Calculated angular distribution of the $^{40}Ca(^{13}C, ^{14}N)^{39}K_{g.s.}$ cross section at an incident energy of 40 MeV as a function of a lower cutoff on the radial integration, R_{co}, for the optical-model parameter set used to calculate the solid curve in Fig. 1. Large contributions to the forward angle cross sections are obtained well inside the channel radius.

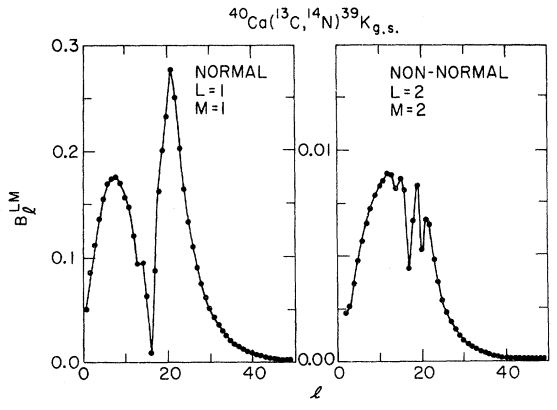

FIG. 3. Transition amplitudes, B_l^{LM}, corresponding to the $M=1$ substate of the normal $L=1$ and the $M=2$ substate of the nonnormal $L=2$ $^{40}Ca(^{13}C, ^{14}N)^{39}K_{g.s.}$ transition. These amplitudes correspond to the calculation whose angular shape is shown as a solid curve in Fig. 1. Large amplitudes are predicted for the low partial waves.

nuclear interior must be increased to reduce what are clearly unphysical contributions; yet it is necessary to maintain a weak absorption in the nuclear surface region to reproduce the large forward angle cross sections observed in the $^{40}Ca(^{13}C, ^{14}N)^{39}K$ ground state transition (see Fig. 1) and elsewhere. Inevitably the imaginary well depth must experience a sharp decrease in the nuclear surface, as one passes from the deep interior to the shallow exterior absorption. Within the framework of one body optical potentials a reasonable prescription is the introduction of an imaginary part possessing two pieces: a volume piece with a small diffusivity to simulate the rapid surface change and a surface piece with a diffusivity equal to that of the real potential. A physical basis for such a potential shape is not hard to find. At separations of projectile-target centers implying large overlap of densities, violent compound reactions must be taking place which destroy the identity of the entrance channel and leave only a small probability for exit into simple direct channels. The onset of such processes as a function of the (decreasing) separation between centers is likely to be sudden. On the other hand exterior absorption will arise from those reactions

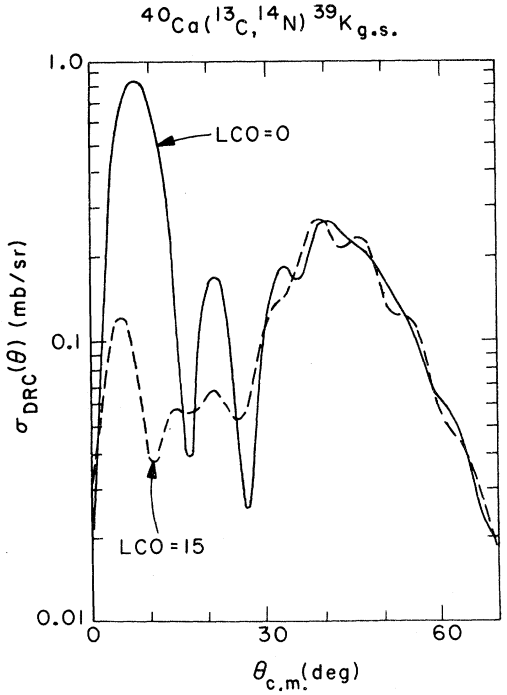

FIG. 4. Comparison of the calculated angular distribution shown as a solid curve with the data in Fig. 1 with an identical calculation (dashed curve labeled LCO=15), having the contributions of the lowest 14 partial waves removed (see Fig. 3).

most probable at larger separation. These are just the direct or quasielastic events which are weaker and fall off with distance at a rate comparable to that seen in the tails of nuclear densities.

In practice we employ a Woods-Saxon volume potential with a diffusivity $a = 0.05$ fm (although as we will point out $a \lesssim 0.20$ fm would produce similar results), in combination with a surface derivative Woods-Saxon piece possessing $a = 0.55$ fm. The explicit form of these potentials and their parametrization is included in Table II (Set 1).

Predictions based on such parameters are shown in Fig. 5 for the ^{40}Ca(^{13}C, ^{14}N) and ^{40}Ca(^{13}C, ^{12}C) transitions to the ground states of ^{39}K and ^{41}Ca.

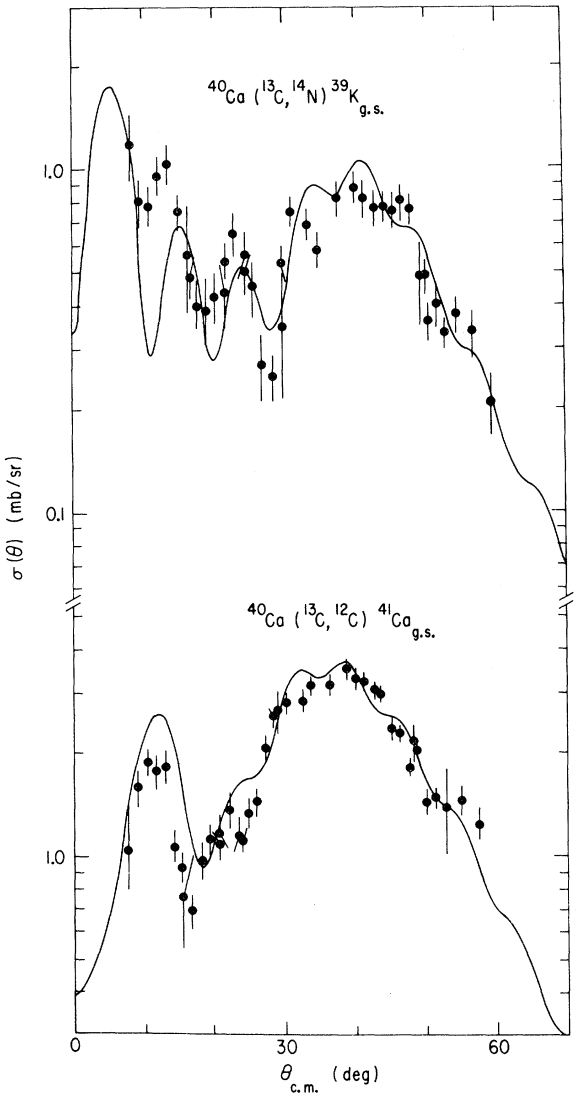

FIG. 5. Comparison of measured (Refs. 25 and 26) and calculated angular distributions for the 40 MeV ^{40}Ca(^{13}C, ^{14}N)^{39}K and ^{40}Ca(^{13}C, ^{12}C)^{41}Ca ground state transitions. The curves were calculated using the proposed optical potentials (given as Set 1 of Table II) which are nearly transparent near the nuclear surface and strongly absorbing in the nuclear interior.

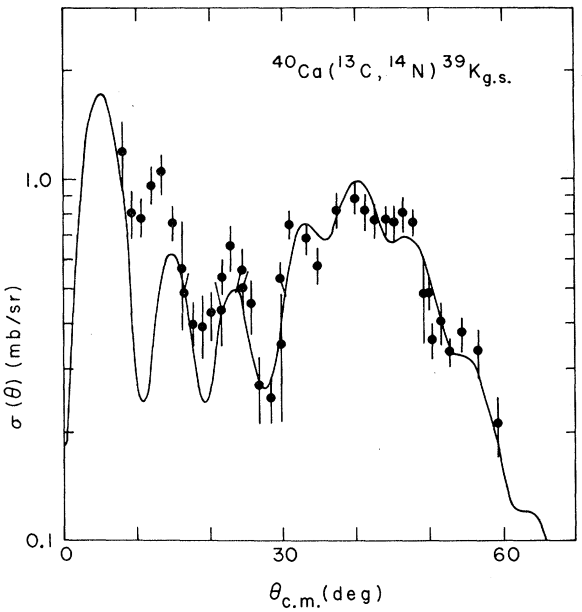

FIG. 6. Comparison of the measured 40 MeV ^{40}Ca(^{13}C, ^{14}N)^{39}K$_{g.s.}$ angular distribution (Refs. 25 and 26) with that calculated using optical potentials having a pure volume absorption with a small diffusivity (Set 3 of Table II).

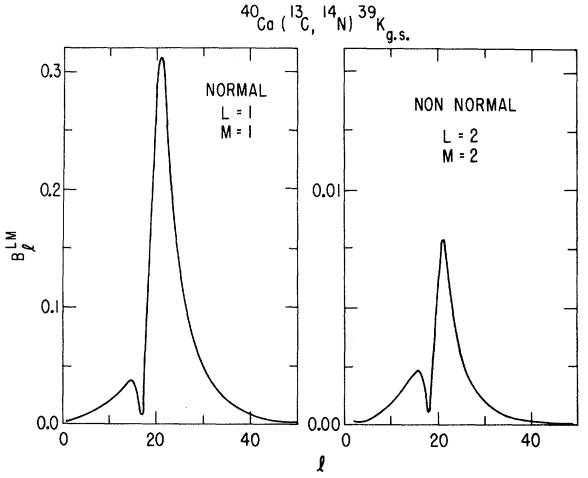

FIG. 7. Transition amplitudes, B_l^{LM}, for the $M = 1$ substate of the normal, $L = 1$ and the $M = 2$ substate of the non-normal, $L = 2$ ^{40}Ca(^{13}C, ^{14}N)^{39}K$_{g.s.}$ transitions calculated using the proposed surface transparent potentials (Set 1 of Table II). The large amplitudes predicted for low partial waves using weak absorptive potentials of Woods-Saxon geometry (Fig. 3) are much reduced.

The theoretical curves in Fig. 5 are normalized by $N = 1.25$ for both the ^{40}Ca(^{13}C, ^{14}N)^{39}K(g.s.) and ^{40}Ca(^{13}C, ^{12}C)^{41}Ca(g.s.) transitions. The spectroscopic factors assumed for such normalization are given in Table I. The shape of the (^{13}C, ^{12}C) angular distribution is well reproduced by these calculations. The general shape of the more structured (^{13}C, ^{14}N) angular distribution is given, but the details of the most forward angle data still are not completely reproduced. However, predictions based on these potentials give a better description of the forward angle ^{40}Ca(^{13}C, ^{14}N)^{39}K(g.s.) data than calculations using potentials with the same real and imaginary Woods-Saxon geometry (see, e.g., Fig. 1).

Optical potentials with purely volume absorption but small diffusivity also are able to reproduce the general features of the ^{40}Ca(^{13}C, ^{14}N)^{39}K ground state transition at 40 MeV (see Fig. 6), and have been used to fit other distributions at higher energies.[6, 10, 11] Although it is generally possible to fit a specific reaction at a single energy with this type of potential, it seems preferable, on physical grounds, to include a surface dissipation with a standard diffusivity. This surface absorption also proves to be very useful in accounting for the observed increase with energy of the imaginary potential.[14]

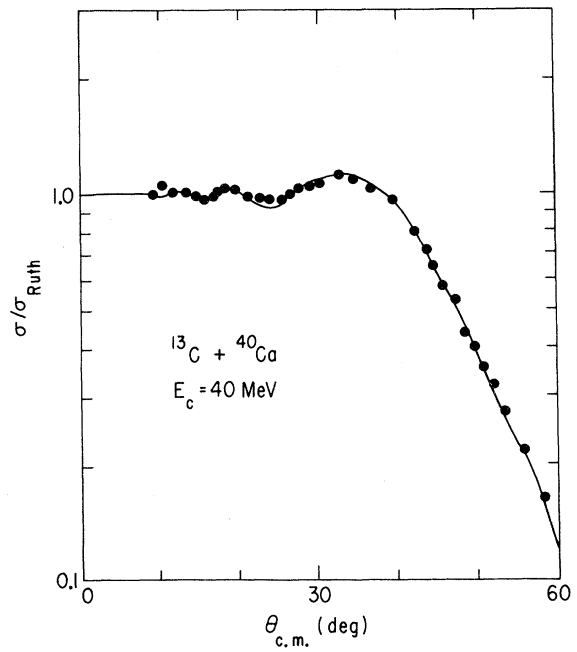

FIG. 8. Comparison of measured (Refs. 25 and 26) and calculated 40 MeV ^{13}C elastic scattering from ^{40}Ca using the proposed surface transparent potentials (Set 1 of Table II) that reproduce the transfer angular distributions (Fig. 5).

The ^{40}Ca(^{13}C, ^{14}N)^{39}K(g.s.) transition amplitudes, β_l^{LM}, calculated for the $M = 1$ normal and $M = 2$ non-normal magnetic substates using the potentials we propose are shown as a function of l in Fig. 7. As a result of the stronger absorption in the nuclear interior, the larger contributions that were observed for the small partial waves using the weakly absorbing Woods-Saxon potentials (see Fig. 3) are greatly reduced in these calculations. In Fig. 8 the 40 MeV ^{13}C elastic scattering from ^{40}Ca predicted using these potentials is compared with experimental data. Here, as elsewhere in the paper, the elastic scattering was not refitted with these potentials, but the calculated elastic cross sec-

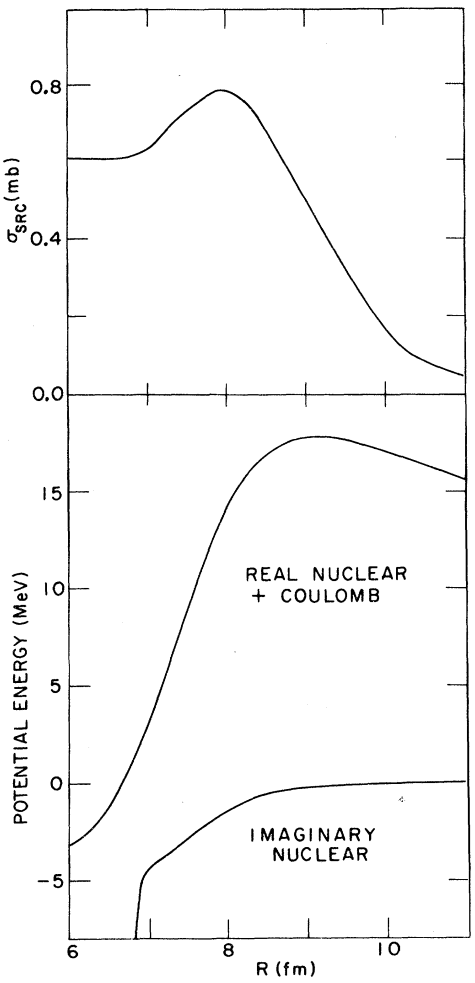

FIG. 9. (Top) Predicted total cross section of the 40 MeV ^{40}Ca(^{13}C, ^{14}N)^{39}K ground state transition as a function of a lower cutoff on the radial integration in the surface region for the proposed surface transparent potentials. (Bottom) The radial shape of the real and imaginary optical potentials also are shown for comparison. The largest contribution to the total cross sections is from the region of the Rutherford radius.

tions do not differ radically from the experimental ones (see Fig. 8).

In Fig. 9 the calculated total cross section for the ^{40}Ca(^{13}C, ^{14}N)^{39}K ground state transition at an incident energy of 40 MeV is shown as a function of a lower cutoff in the radial integration. These calculations used the surface transparent potentials. For comparison, the real nuclear + Coulomb and imaginary nuclear potentials in the ^{13}C + ^{40}Ca channel also are shown. It must be emphasized that the use of a radial cutoff is only heuristic, but it does indicate for what radii large contributions are obtained in the calculated cross sections. The predicted cross sections corresponding to radial cutoffs of $\lesssim$7 fm were nearly identical both in magnitude and shape[14] to the cross section calculated with no radial cutoff. This is in sharp contrast to the weak Woods-Saxon imaginary potential which also produced large forward angle cross sections (Fig. 1), but had significant contributions from the nuclear interior (see Fig. 2). The rise in the total cross section for cutoffs between 7 and 8 fm results from removing certain contributions which caused cancellations in the total cross section. The main contributions to the total cross section are still obtained in the region of the Rutherford (or barrier) radius, where nuclear and Coulomb forces balance, though very weak potentials are used in the region of the nuclear surface.

B. Other data

The volume plus surface potentials are successful in reproducing cross section magnitudes, as well as angular shapes varying from that typical of a grazing collision to ones possessing rapid oscillations. The optical model parameters and spectroscopic factors for all cases considered are given in Tables II and I, respectively. Other pertinent information for these various transitions, e.g., transferred angular momentum, normalization constants, incident energies, excitation energies, etc. are collected in Table III.

The cross section of the ^{40}Ca(^{13}C, ^{12}C)^{41}Ca ground state transitions measured at incident energies of 60 and 68 MeV are observed[3] to oscillate as a function of angle. These angular shapes are compared with the calculated cross sections in Fig. 10. An energy dependence in the imaginary depth in the surface region and a slight adjustment in the imaginary radius is needed to predict the change in the angular shape and magnitude of the cross sections for this transition between 40 and 68 MeV. (See Fig. 5 for the comparison between predicted and measured cross sections at 40 MeV incident energy.) It should be noted, however, that these potentials do not reproduce the details of the ^{40}Ca(^{13}C, ^{14}N) reaction at higher energies. At 40 MeV the agreement between data and theory is satisfactory while at 60 and 68 MeV the over-all shape and magnitude of the angular distribution is reproduced but the oscillations in the data are exactly out of phase with the calculations.[14,28]

The forward angle oscillating cross section predicted[1] for the (^{18}O, ^{16}O) reactions on light even-mass Ni targets recently has been established[7] as

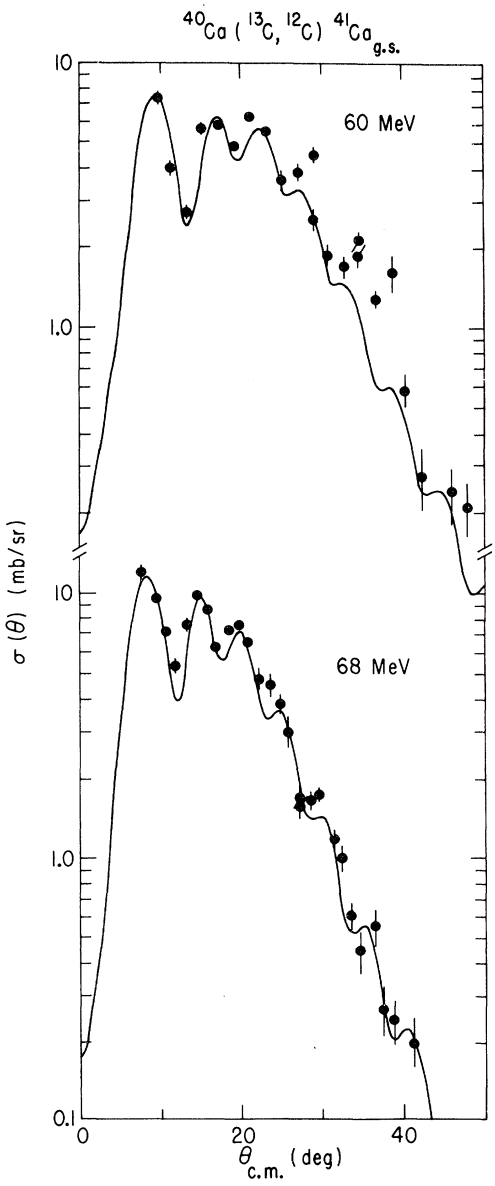

FIG. 10 Comparison of the experimental angular distribution for the ^{40}Ca(^{13}C, ^{12}C)^{41}Ca ground state transition at incident energies of 60 and 68 MeV (Refs. 3 and 28) with DWBA calculations using the proposed surface transparent optical-model parameters given in Table II.

TABLE III. Summary of transitions analyzed.

Reaction	Incident energy (MeV)	Final state E_x (MeV)	J^π	Q (MeV)	Transferred L Normal	Non-normal	Normalization [a] N	Figure [b]	Ref.
^{40}Ca(^{13}C, ^{14}N)^{39}K	40	0.0	$\frac{3}{2}^+$	−0.78	1	2	1.25	5	25
^{40}Ca(^{13}C, ^{12}C)^{41}Ca	40	0.0	$\frac{7}{2}^-$	3.42	4	3	1.25	5	25
	60	0.0	$\frac{7}{2}^-$	3.42	4	3	1.25	10	3
	68	0.0	$\frac{7}{2}^-$	3.42	4	3	1.50	10	3
^{48}Ca(^{14}N, ^{13}C)^{49}Sc	50	0.0	$\frac{7}{2}^-$	2.07	4	3	0.75	14	2
	50	3.08	$\frac{3}{2}^-$	−1.01	2	1	0.75	14	2
^{60}Ni(^{18}O, ^{19}F)^{59}Co	65	0.0 [c]	$\frac{7}{2}^-$	−1.54 [c]	d	d	0.5	13	31
^{60}Ni(^{18}O, ^{16}O)^{62}Ni	65	0.0	0^+	6.23	0	...	...	11	7

[a] Normalization constant N as defined in Eq. (1) for single-nucleon transfer calculations using the sum of Woods-Saxon and surface derivative imaginary potential.

[b] Figure in which calculated cross section shown with data using tabulated normalization.

[c] Assuming ^{19}F in its ground state.

[d] Ground, $J^\pi = \frac{1}{2}^+$; 110 keV, $J^\pi = \frac{1}{2}^-$; and 197 keV, $J^\pi = \frac{5}{2}^+$, final states of ^{19}F not resolved in the experimental data. Calculation includes contributions from all three final states. For ground states normal $L = 3$; for 110 keV state normal $L = 4$ and non-normal $L = 3$; and for 197 keV state normal $L = 1$, 3, and 5 and non-normal $L = 2$ and 4 contribute.

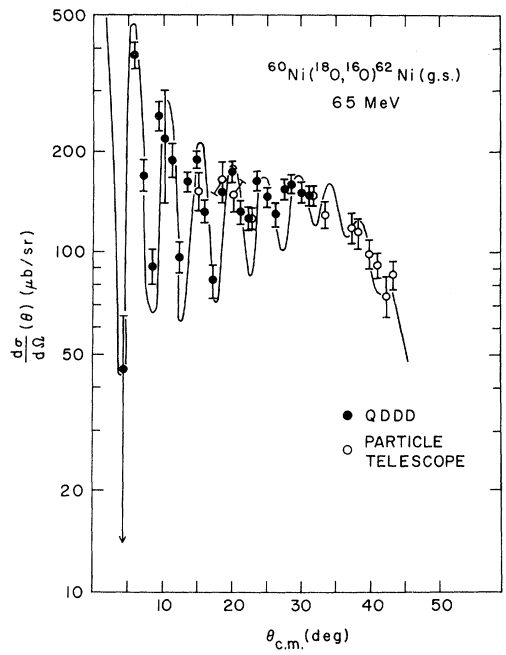

FIG. 11. Comparison of the experimental angular distribution for the ^{60}Ni(^{18}O, ^{16}O)^{62}Ni ground state transition at an incident energy of 65 MeV (Ref. 7) with DWBA calculations using the proposed optical-model parameters given in Table II. For the two-neutron spectroscopic amplitudes listed in Table IV, it was necessary to multiply the calculated cross section by about a factor of 4 to reproduce the absolute magnitude of the measured differential cross sections.

valid for the ^{60}Ni(^{18}O, ^{16}O) transition to the ground state of ^{62}Ni (see Fig. 11). The phase of the oscillations in the experimental cross section again demands that interior contributions must be strongly suppressed (compare the two halves of Fig. 12). The necessity of simultaneously retaining a weak

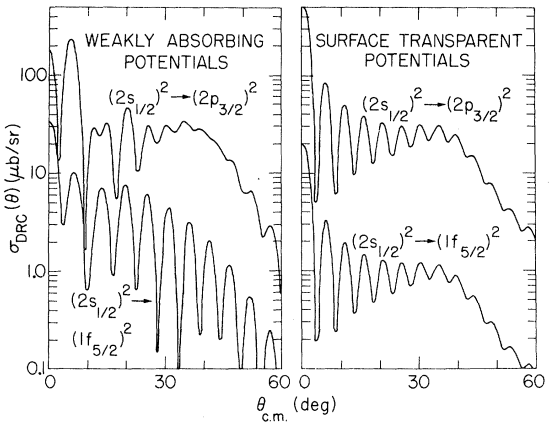

FIG. 12. Comparison of the configuration dependence in the ^{60}Ni(^{18}O, ^{16}O)^{62}Ni$_{g.s.}$ reaction for transfer of a $(2s_{1/2})^2$ neutron pair in ^{18}O$_{g.s.}$ to $(2p_{3/2})^2$ and $(1f_{5/2})^2$ configurations in ^{62}Ni$_{g.s.}$ using the weak volume absorption potentials of Ref. 1 (Set 2 of Table II) and the proposed surface transparent potentials (Set 1 of Table II). The pronounced configuration dependence of the angular shape predicted using the extremely weakly absorbing volume potentials is almost completely removed in the calculations based on the surface transparent potentials for all the configurations listed in Table IV.

TABLE IV. Two-neutron spectroscopic amplitudes used in the ^{60}Ni(^{18}O, ^{16}O)^{62}Ni(g.s.) calculations.

$^{18}O \rightarrow {}^{16}O$ [a]		$^{60}Ni \rightarrow {}^{62}Ni$ [b]	
$(2s_{1/2})^2$	0.450	$(2p_{3/2})^2$	0.795
$(1d_{5/2})^2$	0.893	$(1f_{5/2})^2$	0.991
		$(2p_{1/2})^2$	0.395

[a] Reference 23.
[b] Determined from pairing wave functions of Ref. 29.

absorption at the nuclear surface in order to reproduce the oscillatory structure strongly suggests the type of potential proposed here. The details of the cross section are shown to be reproduced in Fig. 11, using the potential (Set 1) in Table II. These theoretical cross sections were calculated using a proper two-particle form factor[23] and two-neutron spectroscopic amplitudes from the literature[23,29] given in Table IV. Such a calculation underpredicts the magnitude of the cross section by about a factor of 4. Although the effects of recoil may significantly change the calculated absolute cross section,[30] the angular shape should not be appreciably affected. Nearly all of the shape dependence on explicit single-particle configurations, predicted[30] for the ^{60}Ni(^{18}O, ^{16}O)^{62}Ni(g.s.) transition using potentials which were too weakly absorbing in the nuclear interior, is removed in calculations based on potentials which are still nearly surface transparent but are deep in the nuclear interior (see Fig. 12).

The angular shape of the ^{60}Ni(^{18}O, ^{19}F)^{59}Co(g.s.) cross section,[31] measured at the same incident energy of 65 MeV as the ^{60}Ni(^{18}O, ^{16}O)^{62}Ni ground state transition, is reproduced (see Fig. 13) using ^{18}O optical parameters identical to those used in the two-neutron transfer. The same parameters also were used in the ^{19}F exit channel except that the radii were scaled by $A^{1/3}$. The experimental angular distributions contain unresolved particle groups corresponding to ^{19}F in its ground state, $J^\pi = \frac{1}{2}^+$; 110 keV state, $J^\pi = \frac{1}{2}^-$; and 197 keV state, $J^\pi = \frac{5}{2}^+$. The predicted contributions for these three states of ^{19}F scaled by the experimental ^{18}O(^{3}He, d) spectroscopic factors[18] for the corresponding final states of ^{19}F (see Table I) were summed and are shown with the data in Fig. 13. Calculations based on the proposed optical potentials, therefore, reproduce the change in the angular shape from rapidly oscillating forward angle cross sections for the ^{60}Ni(^{18}O, ^{16}O)^{62}Ni(g.s.) transition (Fig. 11) to the shape characteristic of a Coulomb dominated grazing collision for the

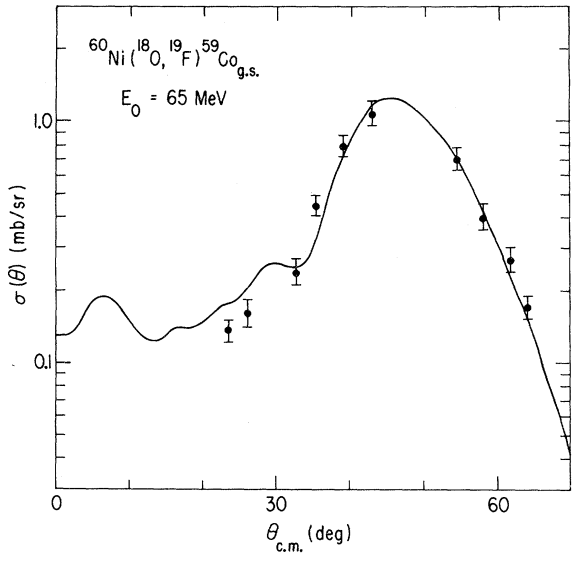

FIG. 13. The angular shape, characteristic of a Coulomb dominated grazing collision, corresponding to the ^{60}Ni(^{18}O, ^{19}F) transition to the ground state of ^{59}Co measured at an incident energy of 65 MeV (from Ref. 31) is reproduced using optical-model parameters (Table II) similar to those which predict rapidly oscillating angular shapes for the ^{60}Ni(^{18}O, ^{16}O)^{62}Ni ground state transitions (see Fig. 11). The ground, 110 keV, and 197 keV states of ^{19}F were not resolved in the experimental data; therefore, the DWBA curve is the sum of the predicted contributions for these states in ^{19}F scaled by the corresponding experimental ^{18}O(^{3}He, d) spectroscopic factors (see Ref. 18 and Table I).

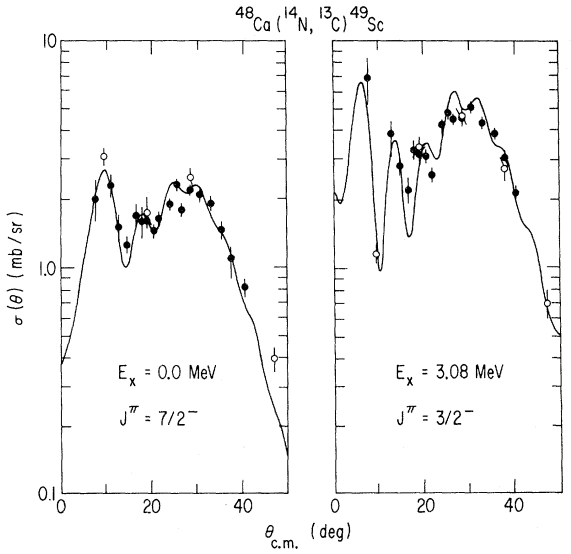

FIG. 14. Comparison of the experimental angular distributions for ^{48}Ca(^{14}N, ^{13}C) transitions to the ground and 3.08 MeV excited states of ^{49}Sc at an incident energy of 50 MeV (Ref. 2) with DWBA predictions using the proposed surface transparent optical-model parameters given in Table II.

^{60}Ni(^{18}O, ^{19}F)^{59}Co reaction (Fig. 13) measured at the same incident energy of 65 MeV.

Large forward angle cross sections have been observed[2] for ^{48}Ca(^{14}N, ^{13}C) transitions to the ground and 3.08 MeV excited state of ^{49}Sc at an incident ^{14}N energy of 50 MeV. Angular distributions of these transitions are shown in Fig. 14. The shapes and magnitudes of these transitions are well reproduced using the potentials given in Table I. These fits are equivalent to the original[2] analysis of this data using weakly absorbing Woods-Saxon potentials.

C. Details of the potential

The shape of the volume Woods-Saxon plus surface derivative imaginary potential proposed for ^{13}C + ^{40}Ca (Set 1 of Table II) is compared in Fig. 15 with a pure Woods-Saxon shape (Set 2 of Table II) that also reproduces the 40 MeV ^{13}C + ^{40}Ca elastic scattering data.[3] Also shown is the sum of the real nuclear and Coulomb potential. Using a pure volume Woods-Saxon imaginary potential with the same geometry as the real potential, it has been impossible to fit the angular distribution of the ^{40}Ca(^{13}C, ^{14}N) transition to the ^{39}K ground state (see Fig. 1). The proposed imaginary potential is weaker than the pure volume form in the nuclear surface region, but it is stronger in the nuclear interior. The strong absorption in the nuclear interior restricts the major contributions for transfer reactions to the region of the nuclear surface. The weaker absorption at the nuclear surface allows the colliding nuclei to be affected by the real nuclear potential, thus enhancing the forward angle cross section. As we have indicated in Sec. III A, if the volume Woods-Saxon imaginary potential is weakened sufficiently to obtain large forward angle cross sections then significant contributions may be obtained from the nuclear interior.

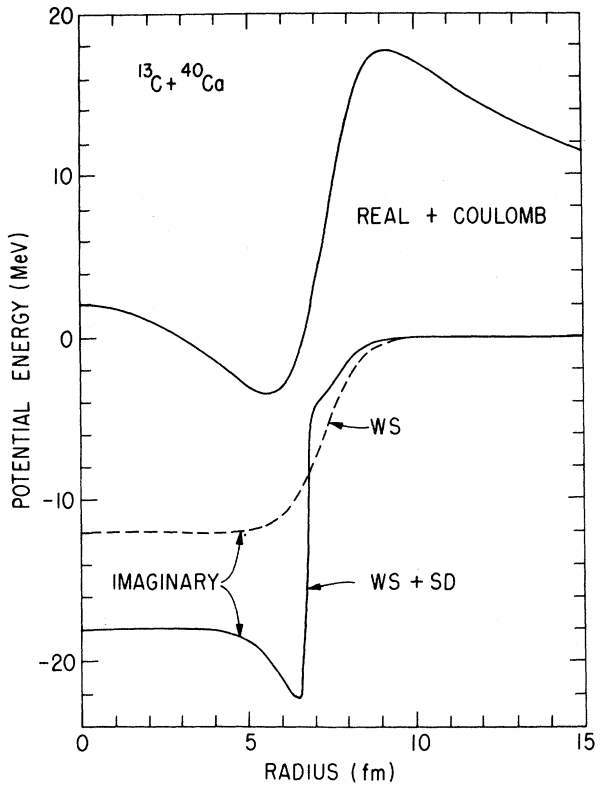

FIG. 15. Comparison of the volume Woods-Saxon plus surface derivative ^{13}C + ^{40}Ca imaginary potential (lower solid curve) given as optical-model Set 1 of Table II with the imaginary part of the pure Woods-Saxon potential (dashed curve)—Set 2 of Table II. Both imaginary potentials together with the same real potential (shown summed with the Coulomb potential as the upper solid curve) reproduce the 40 MeV ^{13}C elastic scattering on ^{40}Ca. Different transfer angular shapes, however, are predicted for the ^{40}Ca(^{13}C, ^{14}N)^{39}K$_{g.s.}$ transition using such potentials (compare the dashed curve of Fig. 1. with the curve of Fig. 5).

The sum of volume and surface derivative shapes in the imaginary potentials possesses a significant feature, a sharp dip at the radius where the Woods-Saxon volume term becomes large. In Fig. 16 calculations for the ^{40}Ca(^{13}C, ^{14}N)^{39}K(g.s.) angular distributions are compared using potentials both with and without such a dip. Nearly no difference is observed between the calculations based on imaginary potentials with this dip and those which are flat inside of the imaginary nuclear radius.

Only five parameters actually have been varied

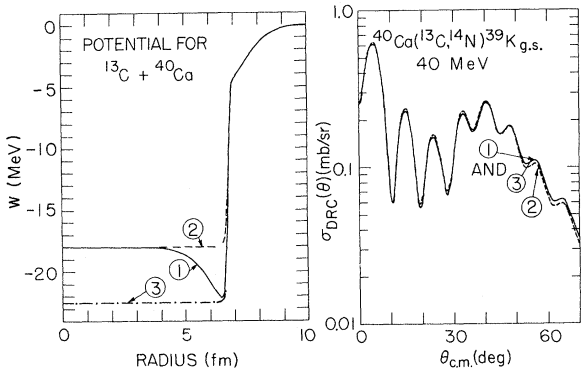

FIG. 16. Comparison of angular shapes (right) corresponding to the ^{40}Ca(^{13}C, ^{14}N)^{39}K ground state transition at an incident energy of 40 MeV for the ^{13}C + ^{40}C imaginary potential shapes shown (left), demonstrating that these cross sections are insensitive to the sharp dip in the imaginary potential labeled 1. The imaginary potential labeled 1 corresponds to parameter Set 1 given in Table II.

to obtain the "fits" shown for these reactions: the real depth, radius, and diffusivity, an imaginary radius and the surface imaginary depth. The depth of the Woods-Saxon part of the imaginary potential has been fixed at about 18 MeV, a value sufficiently large to remove the contribution from the nuclear interior. Equal radii are used in the two portions of the imaginary well (except for the $^{60}Ni + {}^{18}O$ induced cases where the imaginary surface radius arbitrarily was set equal to the real well radius). The diffusivities of the volume and surface derivative parts of the imaginary well have been fixed as $a'_{WS} = 0.05$ fm and $a'_{SD} = a_{real}$ in these calculations. The calculated transfer and elastic angular distributions are relatively insensitive (except at very large angles) to sizeable changes in the depth and diffusivity of the Woods-Saxon part of the imaginary potential so long as this potential is "deep" and has a "sharp" surface. To demonstrate the insensitivity of the calculation to this sharp diffuseness Fig. 17 shows calculations for diffusivities of 0.05, 0.1, and 0.2 in which only the imaginary radius has been changed to reproduce the cross section. It is clear that it would be very difficult to distinguish between these calculations of the transfer cross section based on the existing data. However, a significant difference is predicted in the large angle elastic scattering (Fig. 18), the smallest diffusivities presumably producing more reflection in lower partial waves.

IV. CONCLUSIONS

Certain angular distribution shapes for reasonably low energy heavy-ion induced transfer reactions having both large cross sections at extreme forward angles, and a well formed "bell-shaped" peak at the "grazing" angle are often difficult to reproduce using optical-model potentials with the same Woods-Saxon geometry for both real and imaginary parts of the optical-model potentials. To reproduce such shapes it is necessary to use potentials that are very strongly absorbing in the nuclear interior but are almost transparent near the nuclear surface. A parametrization of such an imaginary potential which is convenient to use and is successful in reproducing both elastic scattering and transfer cross sections is the sum of a deep Woods-Saxon well with a small diffusivity and a shallow surface derivative potential with a diffusivity characteristic of the nuclear matter distribution near the nuclear surface. A similar parametrization for other reactions reproduces both bell-shaped angular distributions characteristic of a grazing collision and rapidly oscillating angular shapes that are observed for higher incident energies. The suggested parametrization seems to be a reasonable one which incorporates the desired exterior and interior features and has a form compatible with existing DWBA and optical-model search codes. However, one could

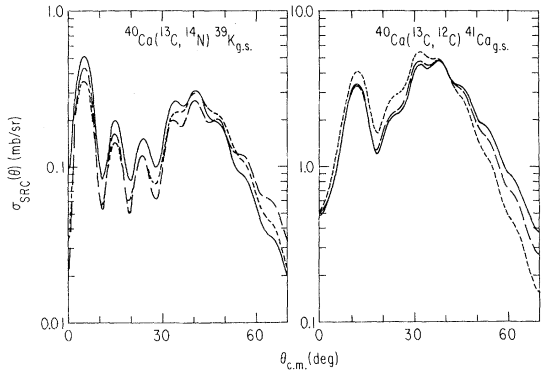

FIG. 17. Comparison of predicted $^{40}Ca(^{13}C, ^{14}N)^{39}K_{g.s.}$ and $^{40}Ca(^{13}C, ^{12}C)^{41}Ca_{g.s.}$ angular shapes (at 40 MeV incident energy) for various diffusivities in the volume part of the imaginary potential. The solid curves, shown with the data in Fig. 5, correspond to parameter Set 1 of Table II having $a'_{ws} = 0.05$ fm. The long dashed and short dashed curves correspond to $a'_{ws} = 0.10$ and 0.20 fm, respectively. The imaginary radius in the ^{14}N channel has been changed to maximize the $(^{13}C, ^{14}N)$ forward angle cross section in these calculations (6.95 fm for $a'_{ws} = 0.10$ fm and 6.85 fm for $a'_{ws} = 0.20$ fm).

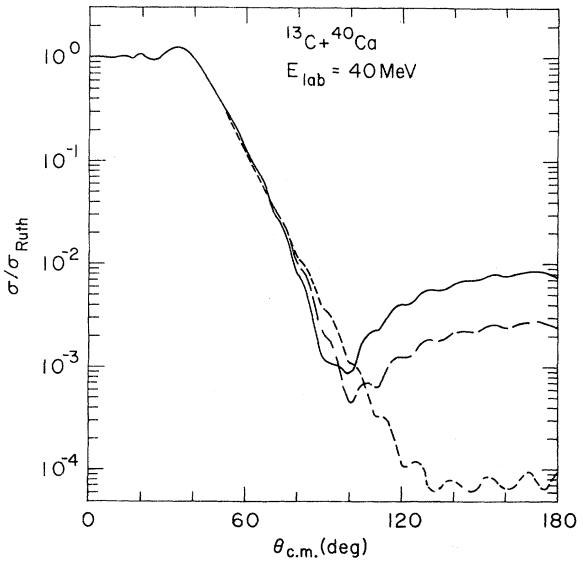

FIG. 18. Comparison of 40 MeV elastic ^{13}C scattering on ^{40}Ca, calculated using parameter Set 1 in Table II with $a'_{ws} = 0.05$ fm (solid curve), 0.10 fm (long dashed curve), and 0.20 fm (short dashed curve). See Fig. 17 for similar comparison on transfer cross sections.

perhaps "draw" a better imaginary potential with these features and without the dip shown in Fig. 15.

The division of absorption into two parts has another distinct advantage. Changes in absorption with energy and channel may be incorporated into the surface depth while leaving the volume depth fixed. One expects such changes to arise more noticeably in the quasielastic connected dissipation, and has in fact been able to describe observed effects in this way.[14,32] In the present work, for example, the surface depth varies strongly between $^{13}C + {}^{40}Ca$ and $^{14}N + {}^{39}K$ and shows some signs of increasing with energy.

Such potentials may have a physical basis with, as we have indicated, the two pieces of absorption almost certainly arising from different processes — compound processes dominating the interior and quasielastic processes important in the region of the nuclear surface. A sharp increase in the absorption might then be expected at the radius where compound processes become important.

We wish to acknowledge the stimulating discussions held with Dr. C. Chasman, Dr. M. J. LeVine, Dr. A. Z. Schwarzschild, Dr. C. E. Thorn, Dr. C. Dover, and Dr. J. Vary.

---

*Work performed under the auspices of the Energy Research and Development Administration.

[1]E. H. Auerbach, A. J. Baltz, P. D. Bond, C. Chasman, J. D. Garrett, K. W. Jones, S. Kahana, M. J. LeVine, M. Schneider, A. Z. Schwarzschild, and C. E. Thorn, Phys. Rev. Lett. 30, 1078 (1973).

[2]M. J. Schneider, C. Chasman, E. H. Auerbach, A. J. Baltz, and S. Kahana, Phys. Rev. Lett. 31, 320 (1973); C. Chasman, S. Kahana, and M. J. Schneider, *ibid.* 31, 1074 (1973).

[3]P. D. Bond, J. D. Garrett, O. Hansen, S. Kahana, M. J. LeVine, and A. Z. Schwarzschild, Phys. Lett. 47B, 231 (1973).

[4]P. R. Christensen, O. Hansen, J. S. Larsen, D. Sinclair, and F. Videbaek, Phys. Lett. 45B, 107 (1973).

[5]P. Braun-Munzinger, W. Bohne, C. K. Gelbke, W. Grochulski, H. L. Harney, and H. Oeschler, Phys. Rev. Lett. 31, 1423 (1973).

[6]W. Henning, D. G. Kovar, B. Zeidman, and J. R. Erskine, Phys. Rev. Lett. 32, 1015 (1974).

[7]M. J. LeVine, A. J. Baltz, P. D. Bond, J. D. Garrett, S. Kahana, and C. E. Thorn, Phys. Rev. C 10, 1602 (1974).

[8]S. Kahana, P. D. Bond, and C. Chasman, Phys. Lett. 50B, 199 (1974).

[9]W. A. Friedman, K. W. McVoy, and G. W. T. Shuy, Phys. Rev. Lett. 33, 308 (1974).

[10]M. C. Mermaz, Saclay report, 1973 (unpublished); see also M.-C. Lemaire, M. C. Mermaz, H. Sztark, and A. Cunsolo, Phys. Rev. C 10, 1103 (1974).

[11]M. S. Zisman, R. M. DeVries, J. G. Cramer, K.-L. Liu, Y-d Chan, and B. Cuengco, Phys. Rev. C 11, 809 (1975).

[12]Preliminary reports of this work are contained in A. Z. Schwarzschild, P. D. Bond, J. D. Garrett, S. Kahana, and M. J. LeVine, Bull. Am. Phys. Soc. 19, 503 (1974); and in Refs. 14 and 25.

[13]W. von Oertzen, C. E. Thorn, A. Z. Schwarzschild, and J. D. Garrett, in *Proceedings of the International Conference on Reactions Between Complex Nuclei, Nashville, Tennessee, June 10–14, 1974,* edited by R. L. Robinson, F. K. McGowan, J. B. Ball, and J. H. Hamilton (North-Holland, Amsterdam, 1974), Vol. I, p. 83; and unpublished.

[14]J. D. Garrett, in *Proceedings of the Symposium on Classical and Quantum Mechanical Aspects of Heavy Ion Collisions, Heidelberg, 1974,* Lecture Notes in Physics Series, edited by H. L. Harney, P. Braun-Munzinger, and C. K. Gelbke (Springer, Berlin, 1975), Vol. 33, p. 59.

[15]A. J. Baltz, Bull. Am. Phys. Soc. 19, 503 (1974); *Proceedings of the International Conference on Reactions Between Complex Nuclei, Nashville, Tennessee, June 10–14, 1974* (see Ref. 13), Vol. I, p. 60. See also J. S. Blair, R. M. De Vries, K. G. Nair, A. J. Baltz, and W. Residorf, Phys. Rev. C 10, 1856 (1974).

[16]A. J. Baltz and S. Kahana, Phys. Rev. C 9, 2243 (1974).

[17]J. Schiffer, G. Morrison, R. Siemssen, and B. Zeidman, Phys. Rev. 164, 1274 (1967).

[18]L. L. Green, C. O. Lennon, and I. M. Naqib, Nucl. Phys. A142, 137 (1970).

[19]K. Seth, J. Picard, and G. R. Satchler, Nucl. Phys. A140, 577 (1970).

[20]S. Raman, Nucl. Data B4, 418 (1970) and references therein.

[21]A. G. Blair and D. D. Armstrong, Phys. Rev. 151, 930 (1966).

[22]S. Cohen and D. Kurath, Nucl. Phys. A101, 1 (1967).

[23]A. J. Baltz and S. Kahana, Phys. Rev. Lett. 29, 1267 (1972).

[24]F. Schmittroth, W. Tobocman, and A. A. Golestaneh, Phys. Rev. C 1, 377 (1970).

[25]P. D. Bond, J. D. Garrett, S. Kahana, M. J. LeVine, and A. Z. Schwarzschild, in *Proceedings of the International Conference on Reactions Between Complex Nuclei, Nashville, Tennessee, June 10–14, 1974* (see Ref. 13), Vol. I, p. 54.

[26]P. D. Bond, C. Chasman, J. D. Garrett, C. K. Gelbke, O. Hansen, M. J. LeVine, A. Z. Schwarzschild, and C. E. Thorn, unpublished.

[27]β_l^{LM} is the coefficient of the Legendre polynomial expansion of the transfer amplitude, specifically,

$$\frac{d\sigma}{d\Omega} = \frac{m_i m_f}{(2\pi\hbar^2)^2}\frac{k_f}{k_i}\frac{(2J_f+1)}{(2J_I+1)}\sum_{LM}\frac{1}{(2L+1)(2S+1)} \times\left|\sum_l \beta_l^{LM} P_l^M \cos\theta\right|^2,$$

where l is the partial wave angular momentum of the final scattering state and L, M are the transferred angular momentum and its projection along the incoming beam axis.

[28]P. D. Bond, J. D. Garrett, O. Hansen, S. Kahana, M. J. LeVine, and A. Z. Schwarzschild, in *Proceedings of the International Conference on Reactions Between Complex Nuclei, Nashville, Tennessee, June 10–14, 1974* (see Ref. 13), Vol. I, p. 55; and unpublished.

[29]L. S. Kisslinger and R. A. Sorensen, K. Dan. Vidensk. Selsk., Mat.—Fys. Medd. 32, No. 9 (1960).

[30]B. F. Bayman, Phys. Rev. Lett. 32, 71 (1974).

[31]E. H. Auerbach, A. J. Baltz, P. D. Bond, C. Chasman, J. D. Garrett, K. W. Jones, S. Kahana, M. J. LeVine, M. Schneider, A. Z. Schwarzschild, and C. E. Thorn, in Proceedings of the Symposium on Heavy-Ion Transfer Reactions, Argonne National Laboratory, March, 1973 [ANL Report PHY-1973B (unpublished)], Vol. II, p. 419.

[32]C. K. Gelbke, J. D. Garrett, M. J. LeVine, and C. E. Thorn, unpublished.